Optical shock-enhanced self-photon acceleration

P. Franke ⬤,[*] D. Ramsey, T. T. Simpson, D. Turnbull, D. H. Froula, and J. P. Palastro ⬤

University of Rochester, Laboratory for Laser Energetics, Rochester, New York 14623, USA

Photon accelerators can spectrally broaden laser pulses with high efficiency in moving electron density gradients driven in a rapidly ionizing plasma. When driven by a conventional laser pulse, the group velocity walk-off experienced by the accelerated photons and deterioration of the gradient from diffraction and plasma refraction limit the extent of spectral broadening. Here we show that a laser pulse with a shaped space-time and transverse intensity profile overcomes these limitations by creating a guiding density profile at a tunable velocity. Self-photon acceleration in this profile leads to dramatic spectral broadening and intensity steepening, forming an optical shock that further enhances the rate of spectral broadening. In this new regime, multi-octave spectra extending from 400 to 60 nm wavelengths, which support near-transform-limited <400 as pulses, are generated over <100 μm of interaction length.

I. INTRODUCTION

Broadband sources of coherent radiation find utility across diverse scientific disciplines as experimental drivers and diagnostic tools. State-of-the-art supercontinuum sources, which primarily achieve spectral broadening through Kerr-induced self-phase modulation of ultrashort laser pulses in either gas-filled fibers [1] or self-guided filaments [2], routinely generate multi-octave spectra in the infrared to ultraviolet wavelength range (15 μm–100 nm) [3–7]. Such sources have thus far been limited to wavelengths >100 nm, due to a lack of dispersion control and strong absorption in the extreme ultraviolet wavelength range ($\lambda = 10$–100 nm). Extending coherent broadband sources into the extreme ultraviolet range would open new wavelength regimes for spectroscopy and increase the achievable spatial and temporal resolution for applications including single-shot spectral interferometry [8], transient spectroscopy [9], and coherence tomography [10]. Photon acceleration, i.e., the continuous increase in frequency accrued by a photon in a temporally decreasing refractive index, offers a promising alternative to Kerr-based supercontinuum sources, with the potential to efficiently generate broadband extreme ultraviolet radiation. A photon accelerated in a rapidly ionizing medium has a frequency ω that evolves in time according to $d\omega^2/dt = \partial\omega_p^2/\partial t$, where $\omega_p \propto \sqrt{n_e}$ is the plasma frequency and n_e is the electron density [11,12]. Maximizing the frequency shift requires the photon to propagate within a sharp electron density gradient over an extended distance. An intense laser pulse can photoionize a dense gas triggering an extremely rapid rise in the electron density. In principle, this allows for large frequency shifts over relatively short interaction lengths. Thus far, however, photon acceleration from optical to extreme ultraviolet frequencies has met with limited success [13–16].

A typical photon accelerator uses a laser pulse focused by conventional optics to drive an axial electron density gradient that moves at the group velocity of the pulse $v_g < c$, where c is the vacuum speed of light [Fig. 1(a)]. Witness photons injected into the gradient undergo a frequency upshift, increasing their group velocity. The resulting group velocity mismatch causes witness photons to outrun, or dephase from the gradient, terminating their frequency increase. Diffraction and plasma refraction cause the drive pulse to diverge from the optical axis, reducing the sharpness of the gradient and the accelerator length, further limiting the maximum frequency shift.

Here we introduce a scheme [Fig. 1(b)] which largely eliminates the adverse effects of diffraction, plasma refraction, and dephasing by combining spatiotemporal [17–22] and transverse intensity profile shaping of the laser pulse [23–25]. This structured flying focus (SFF) pulse has a shaped spatiotemporal profile that creates a far-field intensity peak propagating at a tunable velocity, v_f, over an extended focal range much greater than a Rayleigh length, Z_R. This flying focus effect results from different time slices within the pulse focusing to different positions in the far field. The cylindrically symmetric transverse intensity profile of the SFF increases from a moderate value on the optical axis to a peak at larger radii before falling to zero, so that higher off-axis optical field ionization creates a guiding plasma density profile moving at v_f. This transverse intensity structure is achieved by combining two Laguerre-Gaussian modes in orthogonal polarizations [Fig. 1(d)].

When propagating in a homogeneous partially ionized plasma, a SFF pulse designed such that $v_{g0} < v_f < c$, where v_{g0} is the initial group velocity of the pulse, creates an intensity peak that moves forward within the pulse temporal envelope. The last time slice in the pulse envelope comes to focus first in time, ionizing the background medium. Photons in this initial focus self-accelerate, increasing in frequency and group velocity. These accelerated photons catch up to and remain in phase with the intensity peak formed by the unshifted, downstream photons that are coming into focus later in time. The SFF creates a guiding, radial electron
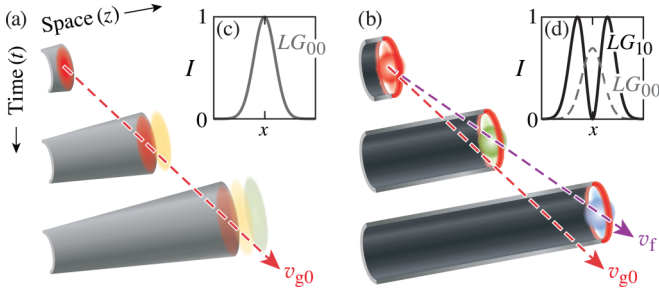
─────────
*pfranke@ur.rochester.edu

FIG. 1. (a) A Gaussian beam drives a (gray) radially convex ionization front at the group velocity of light over approximately a Rayleigh length. Photons diverge from the optical axis due to diffraction and plasma refraction. Frequency upshifted photons dephase from the ionization front due to group velocity walk-off, limiting the system to relatively small frequency shifts. (b) A SFF pulse drives a concave ionization front at a tunable focal velocity $v_f \gtrsim v_{g0}$ over a distance much greater than a Rayleigh length. Photons are concentrated near the optical axis and stay in phase with the ionization front, resulting in many photons undergoing a large frequency shift. Transverse intensity profiles of a typical (c) Gaussian pulse and (d) SFF pulse used in two-dimensional (2D) simulations.

density gradient that dynamically forms just ahead of the central axial density gradient responsible for the photon acceleration. Accelerated photons, thus confined near the optical axis, overlap temporally and spatially with other photons of varying frequency. This local increase in bandwidth and photon density leads to dramatic self-steepening and elevated amplitude of the main intensity peak. The resulting sharpened axial electron density gradient causes faster frequency shifting and more sharpening, which in turn causes even faster frequency shifting. Eventually, optical wave breaking terminates the self-steepening and limits the maximum extent of spectral broadening.

We discover that this self-shocked photon acceleration can generate fully coherent, isolated, 700 as pulses with continuous, multi-octave spectra extending from the 400 nm central wavelength of the incident pulse to <60 nm over <100 μm of interaction length without the need for postcompression. A simple short-pass spectral filter, such as an appropriate metal film [26], can isolate even shorter 350 as pulses with ideal properties, including near-transform-limited duration and high focusability. Under the simulated conditions, only moderate drive pulse energies of 53 μJ and focused intensities of $<5 \times 10^{16}$ W cm^{-2} were required, which would enable the

use of a high-repetition rate, table-top driver with existing laser technology in an experimental realization.

The combination of modest drive laser requirements, relatively high conversion efficiency of 0.12% into <100 nm wavelengths, and the production of isolated attosecond pulses with continuous bandwidths would set a SFF-photon acceleration-based source apart from both gas-based and surface-based high harmonic generation. Such sources typically produce trains of pulses and discrete bandwidths with low efficiency, unless some combination of high pulse energies (mJ–J), high intensities ($>10^{19}$ W cm^{-2}), or complicated gating techniques are used [26–28]. The performance of this scheme is also in contrast to a previous proposal in which photon acceleration driven by a flying focus pulse was successfully used to limit dephasing of the upshifted photons from the ionization front, but was still limited to low efficiencies. (0.001%), accounting for all of the light at the accelerator output [16]. Since the spectrum inferred from photon kinetics simulations in that case showed a minimum wavelength of >90 nm, the efficiency to generate extreme ultraviolet light would be significantly less. The previous scheme required the use of two counterpropagating pulses with dramatically different characteristics that needed to be carefully synchronized and injected into a preformed gas target, further complicating an experimental realization. Here we obtain $100\times$ the energy efficiency, over an accelerator length $100\times$ shorter, and demonstrate broadband, high-intensity subfemtosecond output pulses in a less demanding experimental configuration.

II. RESULTS

Self-photon acceleration of SFF pulses propagating in pre-ionized, underdense nitrogen gas was simulated using a 2D finite-difference time-domain method. The simulation parameters used to obtain all results are shown in Table I. Calculations were limited to the $x - z$ plane, with $\hat{z}$ the pulse propagation direction. The 3D transverse structure of the SFF is a sum of orthogonally polarized Laguerre-Gaussian modes $(LG_{l,p})$, $LG_{00} \hat{x} + LG_{10} \hat{y}$, where l and p are the azimuthal and radial indices respectively. LG_{00} is a typical Gaussian mode, with peak intensity on the optical axis; LG_{10} has zero intensity on axis, which symmetrically increases to a peak off axis in the radial direction. A detailed description of the SFF pulses and their representation in 2D is included in Sec. IV. The $\hat{y}$ component (outside pulse) has higher intensity than the $\hat{x}$ component (inside pulse), such that the optical field ionization rate was high on the optical axis, but increased with

TABLE I. Parameters for simulations shown in each figure. τ is the total full width at half-maximum (FWHM) duration of the pulse, and $\tau_{\rm eff}$ is the FWHM duration of the far-field intensity peak formed by the flying focus. $I_{\rm in}$ and $I_{\rm out}$ are the peak intensities of the inside and outside pulse, respectively. For all simulations, $\lambda_0 = 400$ nm and $F/\# = 6$.

Fig.	v_f/v_{g0}	τ (fs)	$\tau_{\rm eff}$ (fs)	$I_{\rm in}, I_{\rm out}$ ($\times 10^{16}$ W cm^{-2})	n_0 ($\times 10^{20}$ cm^{-3})	Input energy (μJ)
2	1.015	12	3.3	1.2, 4.0	1.5	32
3	1.015	12	3.3	4.0, 4.8	1.5	53
4(a)–4(d)	1.015	12	3.3	4.0, 4.8	1.5	53
4(e)	1.030	30	7.3	4.0, 4.8	6.5	153
4(f)	NA	8.4	NA	4.0, NA	6.5	2.3

absolute transverse coordinate $|x|$ before falling to zero for large $|x|$.

The SFF was spatiotemporally shaped according to the desired ionization front velocity, taking into account the nominal laser group velocity. Each time slice within the temporal pulse envelope had a slightly different electric field radius of curvature and transverse size, such that adjacent time slices of the pulse were focused in succession at adjacent focal positions in the far field with the same diffraction-limited spot size and focused intensity. The initial and final focal lengths within the pulse envelope, and the rate of change between them, were adjusted to produce a focal spot moving at the desired velocity across the extended focal region. The target gas (neutral atomic density $n_0 = 10^{20}$–10^{21} cm^{-3}) was pre-ionized to $Z = 3$, such that the initial electron density of the target was $n_{e0} = 3n_0$. This partial pre-ionization serves three purposes: (1) it reduces the absorption of high-frequency light, (2) it reduces the nominal laser group velocity to $v_{g0} < c$, and (3) it provides a significant level of anomalous (negative) group velocity dispersion. The ionization energies for the third and fourth valence electrons of nitrogen are 47.4 and 77.5 eV, corresponding to wavelengths of 26 and 16 nm. Ionization rates were calculated for 77.5 eV, and Fourier filtering on each time step of the simulation removed wavelengths less than 26 nm to simulate single-photon absorption by triply ionized nitrogen. The maximum ionization state allowed by the model was $Z = 4$. Extending the model to include multilevel ionization could improve results by allowing sharper density gradients to develop and long-distance guiding to be maintained at higher intensities.

The outer pulse of the SFF forms a co-located plasma channel, dynamically guiding the inside pulse (Fig. 2). The outside pulse [Figs. 2(a)–2(c)] and the inside pulse [Figs. 2(d)–2(f)] have the same spatiotemporal shaping and their temporal envelopes have zero delay. Since the outside pulse is more intense, as it comes into focus it reaches the ionization intensity threshold of the background plasma earlier in time and further along the accelerator than the inside pulse. Optical field ionization creates higher off-axis electron density, corresponding to a negative refractive index gradient in the transverse direction. Each slice of the inside pulse comes to focus just inside of the leading edge of this continuously forming optical waveguide. As a result, the guiding structure does not interfere with the propagation of the inside pulse before it comes to focus. Each slice of the inside pulse is prevented from diffracting or refracting from its self-generated plasma only after it reaches focus. This confines the slice to a diffraction-limited transverse size over the remaining length of the channel created by the outside pulse. The piece of the outside pulse that is in focus retains roughly the same shape throughout the entire extent of its propagation, such that the final guiding plasma channel extends over the entire extended focal region of the SFF—nearly five Rayleigh lengths ($Z_R = 18$ μm) [Fig. 2(g)]. The inside pulse begins with high intensity at the back of the pulse envelope [Fig. 2(d)], where, notably, the focal spot size was compressed to 60% of the diffraction limit due to additional focusing by the plasma waveguide. As the high-intensity light at the back of the pulse propagates with a small diameter, the on-axis intensity and electron density increase and steepen [Figs. 2(e) and 2(f)]. The
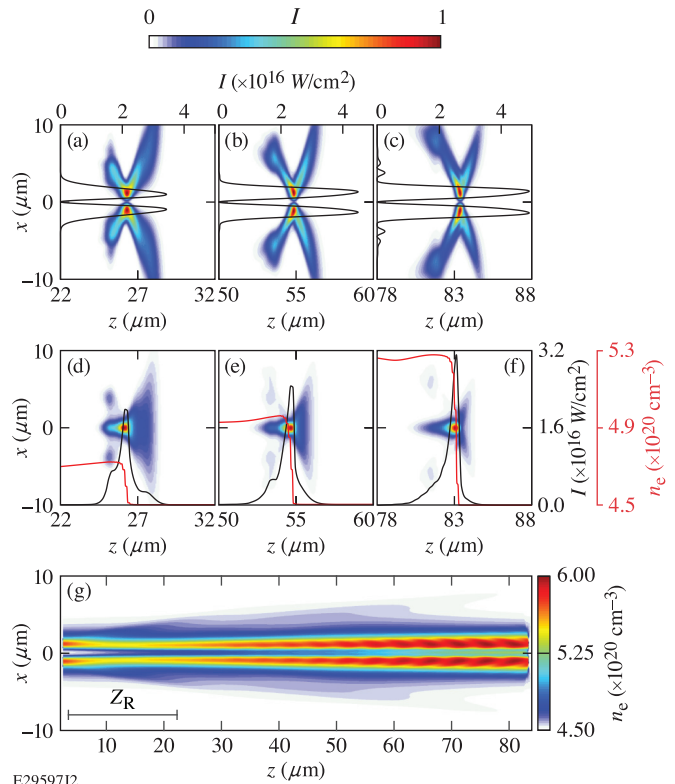

FIG. 2. The outside pulse intensity profiles (color bar) at (a) 96, (b) 192, and (c) 288 fs are shown with the corresponding transverse intensity profile (black) at the maximum intensity in each frame. The inside pulse intensity profiles (color bar) at (d) 96, (e) 192, and (f) 288 fs are shown with the corresponding on-axis electron density (red) and intensity (black) profiles. The color scales were normalized to the peak intensity at each time. (g) The electron density driven by the full SFF pulse after propagating for 288 fs. A guiding channel has formed over $5Z_R$.

effective on-axis duration of the pulse decreased by a factor of 1.6, from 3.3 to 2.0 fs, over only 90 μm. At higher incident intensities, the spot size was only compressed to 80–100% of the diffraction limit, but the duration was compressed $4.7\times$ to 700 as.

The spectrum of the inside pulse evolves rapidly as it propagates along the optical axis [Fig. 3(a)]. Significant broadening about the fundamental frequency was observed within the first 15 μm of interaction length. The spectral width at the 10^{-4} level more than doubled within only 45 μm, and nearly quadrupled within 90 μm. At this point, almost all of the light was shifted to the high-frequency side of the spectrum. Although some ionization-induced odd-harmonic generation was observed [29], comparisons with photon-kinetics simulations, which do not include nonlinear effects [12,30], indicate that it did not play a role in the overall spectral broadening. The spectrum of the inside pulse was radially homogeneous within the diffraction-limited spot ($r_0 = 1.5$ μm), but changed further out due to imperfect guiding at these larger radii. At high intensities, the total duration of the pulse was compressed considerably during the interaction, such that an isolated 700 as pulse was obtained at the accelerator output ($z = 90$ μm) [Fig. 3(b)]. This pulse could

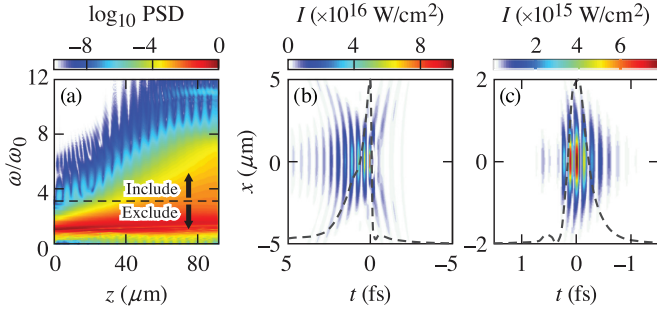FIG. 3. (a) Evolution of the power spectral density (PSD) on the optical axis with interaction length z, where ω_0 is the frequency corresponding to the peak wavelength of the incident pulse, $\lambda_0 = 400$ nm. The black line indicates the position of the short-pass filter applied to all light passing through $z = 90$ μm to obtain the pulse shown in (c). (b) The inside pulse at the output of the accelerator ($z = 90$ μm) with no filtering. (c) The inside pulse at $z = 90$ μm after filtering out all wavelengths >124 nm.
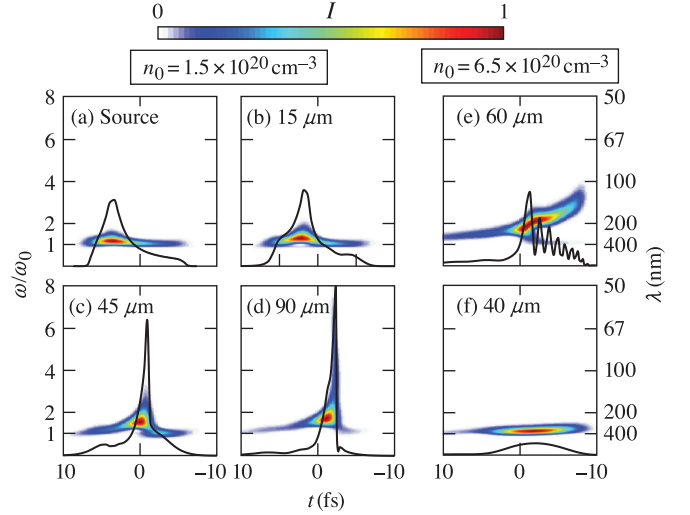

FIG. 4. Spectrograms obtained by wavelet transform of the inside pulse electric field on the optical axis for a SFF pulse at (a) the source input plane, (b) 15 μm, (c) 45 μm, and (d) 90 μm. For comparison, the spectrograms at higher density ($n_0 = 6.5 \times 10^{20}$ cm^{-3}) are shown for (e) a SFF pulse with $v_f = 1.030\,v_{g0} = 0.8740\,c$ and (f) a standard Gaussian pulse. The color scale in each plot is normalized to the peak intensity. On-axis intensity profiles (black) are normalized to 10^{17} W cm^{-2}.

be useful due to its short duration, high intensity, and broad bandwidth; however, it has complicated spatial, spectral, and temporal correlations that could make it unsuitable for certain applications. Applying a simple short-pass filter to the output of the photon accelerator isolates a spatially coherent, extreme ultraviolet pulse [Fig. 3(c)]. The pulse, containing only wavelengths shorter than 124 nm and 0.21% of the total incident pulse energy, has a duration of 1.5 optical cycles, or 350 as intensity full width at half-maximum—1.3 times the transform limit for the filtered bandwidth. With a nearly flat quadratic phase in the transverse direction, the pulse has ideal focusability. Spectral filtering could be achieved by allowing the output pulse to naturally diffract out of the end of the accelerator, collimating it with an appropriate curved reflector [31], and then allowing it to pass through a 200-nm-thick magnesium foil [26]. Finally, the pulse could be refocused through another curved reflector for use in an experiment. The outside pulse undergoes less spectral broadening than the inside pulse, but there is still significant spectral overlap between them. For longer wavelength spectral filter cutoffs ($\gtrsim 150$ nm), a pinhole spatial filter or polarization filter could be used to remove the outside pulse.

The formation of an optical shock drives the extreme refractive index gradients that are responsible for the rapid spectral broadening and temporal compression of the pulse (Fig. 4). The intensity of the incident pulse peaks at the back of the pulse envelope where the first focus occurs [Fig. 4(a)], and the electron density gradient created by this peak induces a frequency upshift of the photons in the initial focus. These photons experience an increase in group velocity due to the anomalous (negative) group velocity dispersion in a plasma, i.e., $v_g = c(1 - \omega_p^2/\omega^2)^{1/2}$. Higher frequencies, initially generated at the back of the pulse, catch up to the unshifted downstream photons, causing a local increase in the intensity and bandwidth, which creates the observed self-steepening and temporal compression.

After 15 μm [Fig. 4(b)], the bandwidth temporally overlapped with the intensity peak at the fundamental frequency has increased. The peak intensity has steepened on the lead-

ing edge and moved forward within the pulse envelope. By 45 μm [Fig. 4(c)], significant local spectral broadening and self-steepening has doubled the peak intensity. At 90 μm [Fig. 4(d)], a temporally localized, extremely broadband signal has developed. Notably, the intensity increases from near zero to its peak in half an optical cycle, indicating that a strong optical shock has formed on the leading edge of the pulse. This time-localized spectral broadening is a unique feature of the self-shocked photon acceleration regime that facilitates attosecond pulse generation without any postaccelerator phase compensation.

For an initial density $4.3\times$ larger than in the previously discussed simulations, the shock catastrophically collapsed over less than 60 μm [Fig. 4(e)]. The spectrogram can be considered a time-velocity phase-space representation, and the observed "folding" of the spectrogram, such that nonadjacent frequencies (velocities) overlap in time, indicates optical wave breaking [32,33]. A strongly modulated intensity profile developed on the leading edge of the pulse, and distinct peaks emerged in the spectrum due to nonlinear four-wave mixing. These two effects terminate the self-steepening and spectral broadening of the main intensity peak by extracting energy and causing deleterious plasma formation.

Figure 4(f) demonstrates the limitations of a standard 8.4 fs Gaussian pulse that was focused at $z = 10$ μm. After 40 μm, the leading edge of the pulse shifted from 400 to 370 nm, but the trailing edge completely diverged from the optical axis due to plasma refraction and diffraction. Refraction and diffraction reduced the peak intensity by $>4\times$, such that ionization and photon acceleration ceased.

Self-steepening of Gaussian pulses was observed in simulations, but the effect was weak compared to the SFF pulse. As the photons' frequency shifted at the peak of the Gaussian
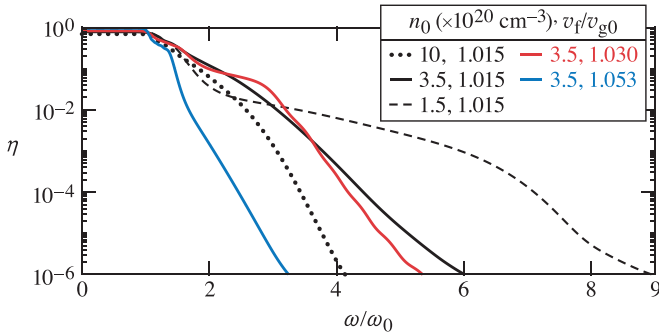
FIG. 5. Parameter scaling of focal velocity v_f and initial density n_0 for a 90 μm accelerator. η is the energy efficiency to produce all light at frequencies above the frequency indicated on the horizontal axis. For all data shown, $I_{\text{in}} = 4.0 \times 10^{16}$ W cm^{-2} and $I_{\text{out}} = 4.8 \times 10^{16}$ W cm^{-2}.

envelope, their increase in group velocity caused them to temporally overlap with the lower-intensity time slices ahead, which were already diffracting out of the focus. This resulted in a small increase in local bandwidth, but no increase in the intensity, such that self-steepening was negligible. For the SFF pulse, photons accelerated in the initial focus were immediately injected into a new high-intensity focus. Each subsequent time slice that came to focus had the original intensity and bandwidth of the pulse, in addition to the accelerated photons, leading to a coherent buildup of intensity and bandwidth. The accelerating gradient was continually pumped by a higher, sharper intensity peak until it collapsed due to wave breaking.

III. DISCUSSION AND CONCLUSION

The exact combination of density and flying focus velocity must be optimized to deliver the greatest bandwidth increase (Fig. 5). Clearly, $v_f \gtrsim v_{g0}$ is optimal for all densities. For $v_f < v_{g0}$, photons focused to shorter focal lengths are contained in earlier time slices of the pulse envelope, and plasma formation prevents the ionization front from propagating continuously over a long distance [34–36]. For $v_f \gg v_{g0}$, photons upshifted at the start of the accelerator do not obtain a large enough group velocity to catch up to the main intensity peak, so a strong shock cannot form.

A target with higher initial density has the potential to reach a higher maximum electron density, in principle supporting sharper density gradients and faster frequency shifting. However, a correspondingly larger initial electron density also yields greater group velocity dispersion and a smaller nominal group velocity, which leads to a shorter wave-breaking distance. At large initial electron density, for the observed optimum $v_f \gtrsim v_{g0}$, the initial intensity peak forms a sharp density gradient and dispersion is strong, quickly accelerating photons to $v_g \gg v_f$. A shock forms and collapses over a short distance since even a small increase in frequency results in a large increase in group velocity, and the initial $v_f \ll c$ is easy to overtake for a photon of higher frequency.

At smaller initial densities, a shallower initial density gradient formed and dispersion was weak, so the shock was formed and sustained over a longer distance. Here a large

increase in frequency resulted in a much smaller increase in group velocity and, since $v_f \lesssim c$, the shifted photons took longer to catch up to, and then dephase from, the intensity peak at the fundamental frequency. The low initial density case leads to larger overall spectral broadening because the shock can build up a density profile with a sharper scale length, sustain its propagation over a longer distance, and remain in phase with accelerated photons over a longer distance than in the high-density case. Notably, the spectrum was less sensitive to the exact v_f at higher densities since initial frequency shifts were larger and dispersion was more significant.

Experimentally, a separate laser pulse could be used to pre-ionize the target through optical field ionization or, alternatively, the plasma could be heated to achieve the desired average ionization state, Z. For the 90 μm accelerator presented here, a longer plasma could be generated, with the interaction only occurring in the first section. Excess energy used in ionizing the unused plasma would decrease the overall energy efficiency by a small factor. An optimal accelerator would require plasmas longer than 90 μm since lower densities and longer acceleration lengths are required for larger frequency shifts. Although small density fluctuations in the target would not appreciably affect the interaction, larger fluctuations could affect the focusing of the pulse, leading to a degradation of the guiding channel driven by the outside beam and ultimately to a lower-quality output pulse.

In summary, a different approach to coherent, broadband radiation generation in the extreme ultraviolet range, enabled by the combination of state-of-the-art pulse shaping methods, was proposed and demonstrated computationally. Optical shock-enhanced self-photon acceleration resulted in coherent spectral broadening to extreme ultraviolet frequencies over a fraction of the distance required in a typical Kerr-based supercontinuum source. Self-compression of the incident pulse was significant, and ideal attosecond pulses could be isolated with a simple short-pass filter. Such a pulse could be useful to enable a single-shot version of the coherence tomography application discussed in Ref. [10] and provide sub-fs time resolution to observe transient effects. A photon accelerator based on SFF driven plasma could be optimized further to deliver higher frequencies, shorter pulses, and better efficiency. By tailoring the initial axial density profile of the target gas and the spatiotemporal shaping together, a shock could be generated at higher densities, accelerating and then stabilizing over long distances at lower densities [37,38], which could enable the generation of shorter extreme ultraviolet wavelengths and possibly a table-top source of coherent soft x rays.

ACKNOWLEDGMENTS

assumes any legal liability or responsibility for the accuracy, completeness, or usefulness of any information, apparatus, product, or process disclosed, or represents that its use would not infringe privately owned rights. Reference herein to any specific commercial product, process, or service by trade name, trademark, manufacturer, or otherwise does not necessarily constitute or imply its endorsement, recommendation, or favoring by the U.S. Government or any agency thereof. The views and opinions of the authors expressed herein do not necessarily state or reflect those of the U.S. Government or any agency thereof. The authors would like to thank J. L. Shaw for fruitful discussions and support.

APPENDIX A: SFF FIELD MODEL

The desired field amplitude to be injected on each time step is calculated analytically using well-known equations of Gaussian optics and simple algebraic equations that govern the desired spatiotemporal and transverse intensity profile characteristics. This calculation method amounts to injecting a Laguerre-Gaussian beam at a single axial position that has time-varying focal length, but constant $F/\#$. This model captures the salient features of a flying focuslike pulse, without reference to a particular spatiotemporal shaping method [17–22].

The field is injected at an axial distance of $z = 0$. Different time slices in the injected pulse are focused to different axial positions, where the shortest focal position is defined as $z = f_s$ and the longest as $z = f_l$. The length of the "extended focal region," which defines the length over which the peak intensity of the pulse will propagate in the far field, is therefore $l = f_l - f_s$. For a pre-ionized target, the initial group velocity is calculated as $v_{g0} = c\sqrt{1 - n_e/n_c(\lambda_0)}$, where n_e is the initial electron density of the target, $n_c(\lambda_0)$ is the critical plasma density for the initial, central wavelength of the injected field, λ_0, and c is the vacuum speed of light.

The field is injected in vacuum just outside the edge of the medium, so that the free space propagation distance is negligible, and the first temporal slice of the pulse is injected at time $t = 0$. The time for the field to propagate from the injection point to $z = f_s$ is $t_s = f_s/v_{g0}$. An inherent delay between field propagating to f_s and f_l within the pulse is denoted Δt, which can take either positive or negative sign, such that the field focusing at f_l arrives there at $t_l = f_l/v_{g0} + \Delta t$. For a constant focal velocity,

$$v_f = \frac{dz}{dt} = \frac{f_l - f_s}{t_l - t_s} = \frac{l}{\frac{l}{v_{g0}} + \Delta t}. \quad (A1)$$

Solving for Δt gives the time required to sweep between focal lengths f_s and f_l,

$$\Delta t = l\frac{v_{g0} - v_f}{v_{g0}v_f}. \quad (A2)$$

Since v_{g0} and l are positive, the sign of Δt depends only on the choice of v_f. Defining f_0 as the focal length injected at $t = 0$,

$$f_0 = \begin{cases} f_l & \text{if } \Delta t < 0 \ (v_f < 0 \text{ or } v_f > v_g) \\ f_s & \text{if } 0 < \Delta t \ (0 < v_f < v_g), \end{cases} \quad (A3)$$

the focal length to be injected as a function of time is given by

$$f(t) = f_0 + \frac{l}{\Delta t}t. \quad (A4)$$

The function $f(t)$ can be used to calculate the full field to be injected at every time step of the simulation for any field that is analytically expressible in terms of the propagation distance z. Here we limit the calculation to the family of Laguerre-Gaussian modes, $LG_{l,p}$, where l and p are the azimuthal and radial indices, respectively. For all $LG_{l,p}$, the far-field beam-waist radius and the Rayleigh length are given by $w_0 = 2\lambda_0(F/\#)/\pi$ and $Z_R = \pi w_0^2/\lambda_0$, respectively. We substitute $f(t)$ for the general focal length f in the well-known equations for the field curvature $R(t) = f(t)\{1 + [Z_R/f(t)]^2\}$, beam radius $W(t) = w_0\{1 + [f(t)/Z_R]^2\}^{1/2}$, and Gouy phase $\psi(t) = \tan^{-1}[f(t)/Z_R]$ such that they are all parametric functions of time.

The full field to be injected as a function of time and transverse coordinates r and θ becomes

$$E(r, \theta, t) = E_0 \frac{w_0}{W(t)} L_p^{|l|}\left[\frac{2r^2}{W^2(t)}\right]$$
$$\times \exp\left[-\frac{r^2}{W^2(t)}\right]\exp\left\{-i\left[\omega t - k\frac{r^2}{2R(t)}\right]\right\}$$
$$\times \exp\{i[l\theta - (1 + |l| + 2p)\psi(t)]\}T(t), \quad (A5)$$

where $L_p^{|l|}$ is the generalized Laguerre polynomial of the order of $|l|$ and p, E_0 is the electric field amplitude at focus, and ω and k are the vacuum frequency and wave number for λ_0. $T(t)$ is a time envelope function, which was chosen to be a super-Gaussian of the order of $g = 8$, centered at $t = t_0$ and with width τ,

$$T(t) = \exp\left\{-\left[\frac{(t - t_0)^2}{2\tau^2}\right]^g\right\}, \quad (A6)$$

where $t_0 = |\Delta t|/2$ and $\tau = \sqrt{8^{-1}\ln(2)^{-1/g}|\Delta t|^2}$. The total energy of the pulse scales with the total pulse duration as $P_0|\Delta t|$, where P_0 is the instantaneous power, such that the incident energy depends on l, v_f, and v_{g0}. The duration of the intensity peak in the focal region is $\tau_{\text{eff}} = 2Z_R/|U|$, where $U = v_g v_f/(v_g - v_f)$, which in 2D becomes $\tau_{\text{eff}} = 2\sqrt{3}Z_R/|U|$.

For 2D simulations, we set $y = 0$ in Eq. (5) and take the prefactor $w_0/W(t) \to \sqrt{w_0/W(t)}$. The spatiotemporal characteristics defined by $f(t)$ were the same for the two polarization states. A mode with $l = p = 0$ was injected with $\hat{x}$ polarization, and a mode with $l = 1$ and $p = 0$ was injected with orthogonal $\hat{y}$ polarization. Since Laguerre-Gaussian modes of unequal order experience a different Gouy phase shift, injecting them in the same polarization yields a transverse intensity profile that evolves with z. Therefore, to maintain the desired guiding-intensity profile for all z, the two modes are injected with orthogonal polarizations so that no interference occurs between them.

In practice, such a pulse could be produced by splitting the Gaussian output of a master oscillator, rotating the polarization of one arm, allowing the other arm to pass through a spiral phase plate [23–25], and then recombining the two arms such that the relative timing between the centers of

the two pulse envelopes is zero. Such splitting and recombining of a pulse from the same laser oscillator can be achieved with small temporal uncertainty, as in a typical Mach-Zehnder interferometer. Small deviations from this cotiming condition are not expected to significantly impact the results. Finally, the recombined pulse could be spatiotemporally shaped using one of the several methods discussed in Refs. [17–22].

APPENDIX B: SIMULATION DETAILS

Electric (**E**) and magnetic (**B**) field evolution was simulated by using Yee's algorithm to solve Maxwell's equations on a two-dimensional grid. Two independent field calculations arise in this numerical scheme, which naturally handles the injection of the orthogonally polarized fields used in the presented simulations. The electron response was calculated using a fluid current model according to $d\mathbf{J}/dt = e^2 n_e \mathbf{E}/m_e$, where $\mathbf{J}$ is the current density, $e < 0$ is the electron charge, m_e is the electron mass, and n_e is the electron density. Ions were

assumed to be immobile due to the short timescales relevant in the interaction.

A cycle de-averaged quasistatic Keldysh model was used to calculate the optical field ionization (OFI) rates for the ionization energies of nitrogen [39,40]. Electromagnetic field depletion due to OFI was accounted for using an effective current related to the OFI rate and ionization energy [41]. Collisional ionization, recombination and Joule heating, and their effects on temperatures, currents, and densities were also included in the model.

Values of the spatial resolution ($\Delta z = \lambda_0/60 = 6.5$ nm and $\Delta x = \lambda_0/30 = 13$ nm) and temporal resolution [$\Delta t = 0.99(c\sqrt{\Delta x^{-2} + \Delta z^{-2}})^{-1} = 19.7$ as] were chosen to resolve the highest frequencies and shortest wavelengths in the simulations, while tightly satisfying the Courant condition to minimize numerical dispersion. A perfectly matched layer at the edges of the simulation domain enforced absorbing boundary conditions. The initial electron density and nitrogen density were linearly increased from 0 to their initial value over 800 nm at all four edges of the target.

[1] J. M. Dudley, G. Genty, and S. Coen, Supercontinuum generation in photonic crystal fiber, Rev. Mod. Phys. **78**, 1135 (2006).

[2] A. Couairon and A. Mysyrowicz, Femtosecond filamentation in transparent media, Phys. Rep. **441**, 47 (2007).

[3] K. Jiao, J. Yao, X. ge Wang, X. Wang, Z. Zhao, B. Zhang, N. Si, J. Liu, X. Shen, P. Zhang, S. Dai, Q. Nie, and R. Wang, 1.2–15.2 μm supercontinuum generation in a low-loss chalcohalide fiber pumped at a deep anomalous-dispersion region, Opt. Lett. **44**, 5545 (2019).

[4] F. Belli, A. Abdolvand, W. Chang, J. C. Travers, and P. S. Russell, Vacuum-ultraviolet to infrared supercontinuum in hydrogen-filled photonic crystal fiber, Optica **2**, 292 (2015).

[5] A. Ermolov, K. F. Mak, M. H. Frosz, J. C. Travers, and P. S. J. Russell, Supercontinuum generation in the vacuum ultraviolet through dispersive-wave and soliton-plasma interaction in a noble-gas-filled hollow-core photonic crystal fiber, Phys. Rev. A **92**, 033821 (2015).

[6] J. C. Travers, T. F. Grigorova, C. Brahms, and F. Belli, Self-focusing and self-compression of intense pulses via ionization-induced spatiotemporal reshaping, Nat. Photon. **13**, 547 (2019).

[7] N. Aközbek, S. A. Trushin, A. Baltuška, W. Fuß, E. Goulielmakis, K. Kosma, F. Krausz, S. Panja, M. Uiberacker, W. E. Schmid, A. Becker, M. Scalora, and M. Bloemer, Extending the supercontinuum spectrum down to 200nm with few-cycle pulses, New J. Phys. **8**, 177 (2006).

[8] H. Mashiko, M.-C. Chen, A. Asaga, A. Oshima, I. Katayama, J. Takeda, T. Nishikawa, and K. Oguri, Spatially resolved spectral phase interferometry with an isolated attosecond pulse, Opt. Express **28**, 21025 (2020).

[9] K. Ramasesha, S. R. Leone, and D. M. Neumark, Real-time probing of electron dynamics using attosecond time-resolved spectroscopy, Annu. Rev. Phys. Chem. **67**, 41 (2016).

[10] F. Wiesner, M. Wünsche, J. Reinhard, J. J. Abel, J. Nathanael, S. Skruszewicz, C. Rödel, S. Yulin, A. Gawlik, G. Schmidl, U. Hübner, J. Plentz, G. G. Paulus, and S. Fuchs, Material-specific

imaging of nanolayers using extreme ultraviolet coherence tomography, Optica **8**, 230 (2021).

[11] S. C. Wilks, J. M. Dawson, W. B. Mori, T. Katsouleas, and M. E. Jones, Photon Accelerator, Phys. Rev. Lett. **62**, 2600 (1989).

[12] J. T. Mendonça, *Theory of Photon Acceleration* (IOP, Bristol, UK, 2001).

[13] J. M. Dias, N. C. Lopes, L. O. Silva, G. Figueira, J. T. Mendonça, C. Stenz, F. Blasco, A. Dos Santos, and A. Mysyrowicz, Photon acceleration of ultrashort laser pulses by relativistic ionization fronts, Phys. Rev. E **66**, 056406 (2002).

[14] N. C. Lopes, G. Figueira, J. M. Dias, L. O. Silva, J. T. Mendonça, P. Balcou, G. Rey, and C. Stenz, Laser pulse frequency up-shifts by relativistic ionization fronts, Europhys. Lett. **66**, 371 (2004).

[15] J. M. Dias, C. Stenz, N. Lopes, X. Badiche, F. Blasco, A. Dos Santos, L. Oliveira e Silva, A. Mysyrowicz, A. Antonetti, and J. T. Mendonça, Experimental Evidence of Photon Acceleration of Ultrashort Laser Pulses in Relativistic Ionization Fronts, Phys. Rev. Lett. **78**, 4773 (1997).

[16] A. J. Howard, D. Turnbull, A. S. Davies, P. Franke, D. H. Froula, and J. P. Palastro, Photon Acceleration in a Flying Focus, Phys. Rev. Lett. **123**, 124801 (2019).

[17] D. H. Froula, D. Turnbull, A. S. Davies, T. J. Kessler, D. Haberberger, J. P. Palastro, S.-W. Bahk, I. A. Begishev, R. Boni, S. Bucht, J. Katz, and J. L. Shaw, Spatiotemporal control of laser intensity, Nat. Photon. **12**, 262 (2018).

[18] A. Sainte-Marie, O. Gobert, and F. Quere, Controlling the velocity of ultrashort light pulses in vacuum through spatiotemporal couplings, Optica **4**, 1298 (2017).

[19] J. P. Palastro, J. L. Shaw, P. Franke, D. Ramsey, T. T. Simpson, and D. H. Froula, Dephasingless Laser Wakefield Acceleration, Phys. Rev. Lett. **124**, 134802 (2020).

[20] C. Caizergues, S. Smartsev, V. Malka, and C. Thaury, Phase-locked laser-Wakefield electron acceleration, Nat. Photon. **14**, 475 (2020).

[21] T. T. Simpson, D. Ramsey, P. Franke, N. Vafaei-Najafabadi, D. Turnbull, D. H. Froula, and J. P. Palastro, Nonlinear spatiotemporal control of laser intensity, Opt. Express **28**, 38516 (2020).

[22] H. E. Kondakci and A. F. Abouraddy, Optical space-time wave packets having arbitrary group velocities in free space, Nat. Commun **10**, 929 (2019).

[23] M. Beijersbergen, R. Coerwinkel, M. Kristensen, and J. Woerdman, Helical-wavefront laser beams produced with a spiral phaseplate, Opt. Commun. **112**, 321 (1994).

[24] Y. Shen, X. Wang, Z. Xie, C. Min, X. Fu, Q. Liu, M. Gong, and X. Yuan, Optical vortices 30 years on: Oam manipulation from topological charge to multiple singularities, Light Sci. Appl. **8**, 90 (2019).

[25] A. Longman, C. Salgado, G. Zeraouli, J. I. A. naniz, J. A. Pérez-Hernández, M. K. Eltahlawy, L. Volpe, and R. Fedosejevs, Off-axis spiral phase mirrors for generating high-intensity optical vortices, Opt. Lett. **45**, 2187 (2020).

[26] G. D. Tsakiris, K. Eidmann, J. Meyer-ter-Vehn, and F. Krausz, Route to intense single attosecond pulses, New J. Phys. **8**, 19 (2006).

[27] B. Dromey, M. Zepf, A. Gopal, K. Lancaster, M. S. Wei, K. Krushelnick, M. Tatarakis, N. Vakakis, S. Moustaizis, R. Kodama, M. Tampo, C. Stoeckl, R. Clarke, H. Habara, D. Neely, S. Karsch, and P. Norreys, High harmonic generation in the relativistic limit, Nat. Phys. **2**, 456 (2006).

[28] G. Sansone, L. Poletto, and M. Nisoli, High-energy attosecond light sources, Nat. Photon. **5**, 655 (2011).

[29] F. Brunel, Harmonic generation due to plasma effects in a gas undergoing multiphoton ionization in the high-intensity limit, J. Opt. Soc. Am. B **7**, 521 (1990).

[30] L. Oliveira e Silva and J. T. Mendonça, Kinetic theory of photon acceleration: Time-dependent spectral evolution of ultrashort laser pulses, Phys. Rev. E **57**, 3423 (1998).

[31] C. Bourassin-Bouchet, M. M. Mang, F. Delmotte, P. Chavel, and S. de Rossi, How to focus an attosecond pulse, Opt. Express **21**, 2506 (2013).

[32] W. J. Tomlinson, R. H. Stolen, and A. M. Johnson, Optical wave breaking of pulses in nonlinear optical fibers, Opt. Lett. **10**, 457 (1985).

[33] J. E. Rothenberg and D. Grischkowsky, Observation of the Formation of an Optical Intensity Shock and Wave Breaking in the Nonlinear Propagation of Pulses in Optical Fibers, Phys. Rev. Lett. **62**, 531 (1989).

[34] J. P. Palastro, D. Turnbull, S.-W. Bahk, R. K. Follett, J. L. Shaw, D. Haberberger, J. Bromage, and D. H. Froula, Ionization waves of arbitrary velocity driven by a flying focus, Phys. Rev. A **97**, 033835 (2018).

[35] D. Turnbull, P. Franke, J. Katz, J. P. Palastro, I. A. Begishev, R. Boni, J. Bromage, A. L. Milder, J. L. Shaw, and D. H. Froula, Ionization Waves of Arbitrary Velocity, Phys. Rev. Lett. **120**, 225001 (2018).

[36] P. Franke, D. Turnbull, J. Katz, J. P. Palastro, I. A. Begishev, J. Bromage, J. L. Shaw, R. Boni, and D. H. Froula, Measurement and control of large diameter ionization waves of arbitrary velocity, Opt. Express **27**, 31978 (2019).

[37] L. Oliveira e Silva and J. T. Mendonça, Photon acceleration in superluminous and accelerated ionization fronts, IEEE Trans. Plasma Sci. **24**, 316 (1996).

[38] D. Ramsey, P. Franke, T. T. Simpson, D. H. Froula, and J. P. Palastro, Vacuum acceleration of electrons in a dynamic laser pulse, Phys. Rev. E **102**, 043207 (2020).

[39] L. V. Keldysh, Ionization in the field of a strong electromagnetic wave, Sov. Phys. JETP **20**, 1307 (1964).

[40] G. L. Yudin and M. Y. Ivanov, Nonadiabatic tunnel ionization: Looking inside a laser cycle, Phys. Rev. A **64**, 013409 (2001).

[41] G. M. Petrov and J. Davis, Interaction of intense ultra-short laser pulses with dielectrics, J. Phys. B: At., Mol. Opt. Phys. **41**, 025601 (2008).